Photophysical studies on lanthanide(iii) chelates conjugated to Pittsburgh compound B as luminescent probes targeted to Aβ amyloid aggregates

Alexandre Oliveira, Telma Costa, Licinia Justino, Rui Fausto, Jean-François Morfin, Éva Tóth, Carlos Geraldes, Hugh Burrows

ARTICLE

Received 00th January 20xx,

Accepted 00th January 20xx

DOI: 10.1039/x0xx00000x

Photophysical studies on lanthanide(III) chelates conjugated to Pittsburgh compound B as luminescent probes targeted to Aβ amyloid aggregates

Alexandre C. Oliveira,[a] Telma Costa,[a] Licinia L. G. Justino,[a] Rui Fausto,[a] Jean-François Morfin,[b] Éva Tóth,[b] Carlos F. G. C. Geraldes,[a,c,d*] Hugh D. Burrows[a]*

The photophysical properties of Eu^{3+} and Tb^{3+} complexes of DOTAGA and DO3A-monoamide conjugates of the Pittsburgh compound B (PiB) chromophore, prepared using linkers of different lengths and flexibilities, and which form stable negatively charged (LnL1), and uncharged (LnL2) complexes, respectively, were studied as potential probes for optical detection of amyloid aggregates. The phenylbenzothiazole (PiB) moiety absorbs light at wavelengths longer than 330 nm with a high molar absorption coefficient in both probes, and acts as an antenna in these systems. The presence of the luminescent Ln^{3+} ion quenches the excited states of PiB through an energy transfer process from the triplet state of PiB to the metal centre, and structured emission is seen from Eu^{3+} and Tb^{3+}. The luminescence study indicates the presence of a $^5D_4 \rightarrow T_1$ back transfer process in the Tb^{3+} complexes. It also provides insights on structural properties of the Eu^{3+} complexes, such as the high symmetry environment of the Eu^{3+} ion in a single macrocyclic conformation and the presence of one water molecule in its inner coordination sphere. The overall quantum yield of luminescence of EuL1 is higher than for EuL2. However, their low values reflect the low overall sensitization efficiency of the energy transfer process, which is a consequence of the large distances between the metal center and the antenna, especially in the EuL2 complex. DFT calculations confirmed that the most stable conformation of the Eu^{3+} complexes involves a combination of a square antiprismatic (SAP) geometry of the chelate and an extended conformation of the linker. The large calculated average distances between the metal center and the antenna point to the predominance of the Förster energy transfer mechanism, especially for EuL2. This study provides insights into the behavior of amyloid-targeted Ln^{3+} complexes as optical probes, and contributes towards their rational design.

Keywords: Aβ amyloid, Eu(III) and Tb(III) luminescent probes, DOTAGA, Pittsburgh compound B, DFT calculations.

1. Introduction

Alzheimer's disease (AD) is one of the most frequent disorders in elderly individuals, characterized by progressive neural degeneration causing devastating cognitive impairment.[1,2] Its prevalence increases gradually from about 5% at 65 years to 30% at 85 years old.[3] The two major neuropathological hallmarks of AD are neurofibrillary tangles (NFT) and extracellular amyloid β plaques (Aβ). The amyloid cascade hypothesis assumes that Aβ plaques, which start to form about 10 to 20 years before the first clinical symptoms of the disease, are responsible for the patient's impairment and death.[4] They are insoluble extracellular deposits, mainly composed of the $Aβ_{1-40}$ and $Aβ_{1-42}$ peptides cleaved from the amyloid precursor protein (APP) overexpressed in the disease, which block the synaptic cleft. However, there is evidence indicating that toxicity in AD is caused by intermediate soluble aggregates, such as oligomers and protofibrils, rather than by the amyloid plaques, probably due to their interaction with biological membranes.[5–7]

In only 5% of AD cases, is the disease autosomal dominant[3] due to specific mutations,[8,9] and the diagnosis of this familiar form is easily obtained by identification of these mutations. However, in the dominant 95% sporadic AD cases final diagnosis is only obtained by post-mortem brain histological detection of amyloid plaques using a dye which selectively binds to them.[10]

[a] *University of Coimbra, Coimbra Chemistry Centre (CQC), Department of Chemistry, 3004-535 Coimbra, Portugal*
[b] *Centre de Biophysique Moléculaire, CNRS, UPR 4301, Université d'Orléans, Rue Charles Sadron, 45071 Orléans Cedex 2, France*
[c] *University of Coimbra, Department of Life Sciences, Calçada Martim de Freitas, 3000-393 Coimbra, Portugal*
[d] *CIBIT/ICNAS - Instituto de Ciências Nucleares Aplicadas à Saúde, Pólo das Ciências da Saúde, Azinhaga de Santa Comba, 3000-548 Coimbra, Portugal*
*Address correspondence to:
Carlos F. G. C. Geraldes, Department of Life Sciences, University of Coimbra, Calçada Martim de Freitas, 3000-393 Coimbra, Portugal; Tel. +351239240730; Email: geraldes@ci.uc.pt
Hugh D. Burrows, Department of Chemistry, University of Coimbra, 3004-535 Coimbra, Portugal; Email: burrows@ci.uc.pt

Electronic supplementary information (ESI) available: Fig. S1 - Absorption, fluorescence spectra, fluorescence excitation spectra of the ligands; Fig. S2- Fluorescence decay profiles and their fitting for the ligands and their La^{3+}, Eu^{3+} and Tb^{3+} complexes; Fig. S3 - Absorption spectra of ligands in PBS obtained at increasing irradiation times at 350 nm; Fig. S4 – Absorption, luminescence excitation and luminescence spectra of the Tb^{3+} complexes in PBS, collected with excitation wavelengths of 330 nm and 360 nm, respectively, at T = 298 K. See DOI: 10.1039/x0xx00000x

Current clinical diagnosis is based on cognitive tests, only effective in advanced stages showing evident cognitive decline. The development of imaging probes for *in vivo* detection of the amyloid plaques could allow early diagnosis of AD and provide possibilities of monitoring new therapeutic strategies.[7] A major hurdle in the development of probes and drugs for the central nervous system is the difficulty of crossing the blood-brain barrier (BBB) to reach the brain parenchyma. Some empirical rules have been listed, indicating that the compounds should have low molecular mass and a good lipid solubility.[11,12] In some cases, such as brain cancer, the BBB is weakened and can be readily permeable.[13] It can also be artificially disrupted by hyperosmotic solutions using mannitol, a vasoactive compound. However, this approach can only be used in studies of animal models. Other delivery strategies have used ultrasound and micro-bubbles for transiently opening the BBB. Brain delivery of an imaging probe can be also increased by covalently conjugating it to natural polyamines, such as putrescine, spermine or spermidine, or using lipid soluble agents, carrier proteins, or proteins that can be transported by mediator receptors involved in endocytosis and transcytosis mechanisms.[14]

In the field of *in vivo* imaging of AD, the most significant progress so far has been the development of radiolabeled small-molecule agents capable of entering the brain and specifically targeting plaques and tangles, and their detection by positron emission tomography (PET) or single-photon emission computerized tomography (SPECT). Some small organic molecules, such as benzothiazoles and stilbenes, labeled with the positron emitters ^{18}F or ^{11}C, have shown good affinity towards amyloid aggregates, accompanied by efficient BBB crossover.[15–17] [^{18}F]Florbetapir was the first radiopharmaceutical approved, in 2012, by the FDA for the specific detection of amyloid deposits by PET.[18] Another radiopharmaceutical widely tested for this purpose is the benzothiazole Pittsburg compound B (PiB) labeled with ^{11}C. This Thioflavin T (ThT) derivative is currently in phase 3 clinical trials for PET detection and treatment monitoring of AD.[19] These molecules are used as standards for comparison with other potential biomarkers for PET detection.[20] The PET detection of amyloid plaques using [^{11}C]PIB and [^{18}F]Florbetapir has shown the capability to differentiate between patients having a mild cognitive impairment and those having high risk of developing AD.[21,22] Another approach uses a metal ion radioisotope complexed by a suitable ligand, which is coupled via a spacer to an amyloid-targeting moiety.[23] Several ^{68}Ga-based probes have been reported recently, including conjugates of ^{68}Ga(III) complexes of DOTA (1,4,7,10- tetraazacyclo-dodecane-1,4,7,10-tetraacetic acid) or DTPA (diethylenetriaminepentaacetic acid), exhibiting high in vitro affinity for Aβ aggregates and fibrils, but with very limited brain uptake in *in vivo* AD animal models.[22,24-26] Other reported potential Aβ-targeted PET probes are based on ^{64}Cu-labeled bifunctional chelates conjugated to stilbenes,[27] as well as ^{99m}Tc-based complexes for SPECT detection,[28–31] some of which showed reasonable brain uptake and affinity towards β-amyloid plaques.

Several Magnetic Resonance Imaging (MRI) contrast agents (CAs) have also been developed, based on iron oxide nanoparticles or Gd^{3+} complexes conjugated to the Aβ peptide, intact or covalently bound to a polyamine,[32–35] or to PiB,[36–39] as vectors to target the amyloid aggregates. However, this approach is limited by low BBB permeability of the probes in animal models.

Optical imaging is a sensitive technique with detection in the picomolar probe concentration range. This can be used alone or combined with other modalities, such as MRI or computer tomography (CT). Congo Red (CR) and ThT are commonly used for specific staining of amyloid plaques in *post-mortem* examinations.[20] Luminescent probes also show considerable potential for *in vivo* imaging applications. The requirements for an efficient luminescent agent for AD involve good optical properties, low toxicity and capability of crossing the BBB and targeting plaques. The charged dyes CR and ThT do not cross the BBB *in vivo*, as opposed to their neutral analogues Chrysamine G (CG)[40] and PiB.[19] Conjugated polymers, oligomers and polyelectrolytes show excellent properties for detecting amyloid aggregates.[41] For example, luminescent conjugated polymers have been shown to detect discrete structural differences between protein aggregates, possibly associated with conformational changes on their backbones,[42] while oligothiophenes have been used for *in vitro* and *in vivo* imaging of protein aggregates in cerebral amyloidosis.[43,44] These oligomers may also be useful as therapeutic agents for reducing the pool of toxic species.[45] Luminescent metal complexes also show considerable potential both as optical probes to detect amyloid aggregation and as inhibitors of amyloid formation.[27] Examples include dipyridophenazine ruthenium(II),[46] which is not luminescent in aqueous solution, but shows a strong photoluminescence in the presence of Aβ fibril aggregates.

The main drawback of optical imaging is that light, especially in the UV/Vis region, does not penetrate deeply into tissues, due to light absorption and auto-fluorescence, such that this technique is useful mainly for superficial tissues. Lanthanide complexes show excellent luminescence properties, with spectra consisting of sharp peaks characteristic of each Ln^{3+} ion, involving electronic states with long lifetimes in the μs-ms range, which makes them good choices as optical probes for a variety of chemical and biological systems.[47,48] Their long lifetimes allow the development of time-resolved techniques to eliminate scattering and the short-lived fluorescence background. The major problems with Ln^{3+} ions as optical probes are their low intrinsic molecular absorption coefficients, which can be overcome by the design of efficient organic antennae for sensitized Ln^{3+} based luminescence.[49] The Ln^{3+} luminescence covers a wide spectral range, such as the UV region for Gd^{3+} complexes, which is not biologically useful, and the UV/Vis for Eu^{3+} and Tb^{3+}. Recently, Ln^{3+} ions emitting in the near infrared (NIR), such as Er^{3+} and Yb^{3+}, have generated great interest, especially when using sensitized luminescence with absorption and emission in the NIR region.[50] This minimizes tissue background scattering and auto-fluorescence resulting from the direct excitation of biological constituents like

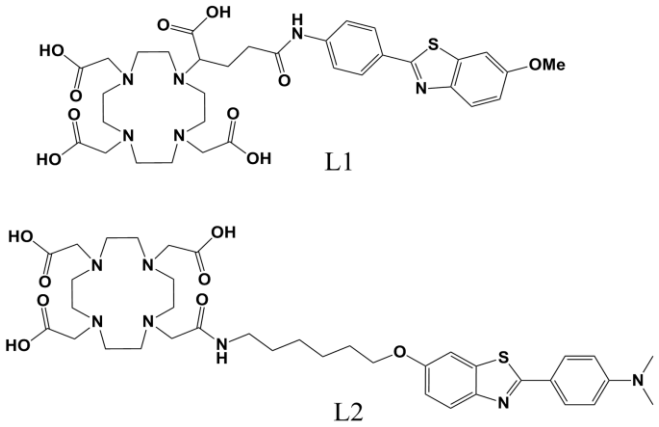

Figure 1 - Chemical structures of ligands **L1** and **L2**.

hemoglobin, making possible the signal detection of deeper tissues in the spectral window between 650 to 1350 nm (the so-called therapeutic window), where human tissues have higher light transmission.[51–53]

In the present work, we report the potential of the Eu^{3+} and Tb^{3+} complexes of two previously reported macrocyclic ligands (L1 and L2) (Figure 1) as probes for optical imaging of aggregated beta amyloid peptides. The ligand L1 is a H_5DOTAGA (1,4,7,10-tetraazacyclo-dodecane-1,4,7-triacetic acid-10-glutaric acid) chelator conjugated with the PiB molecule through its amino group, forming negatively charged lanthanide complexes (LnL1) at physiologically relevant pH values.[54] L2 is a DO3A-monoamide derivative conjugated to the hydroxyl group of PiB, forming neutral lanthanide complexes (LnL2).[55] The L1 and L2 chelators are expected to form thermodynamically very stable and kinetically inert complexes with Ln^{3+} ions. Gd^{3+} complexes of ligands of these types have been extensively studied as potential MRI contrast agents and some of their radiolabeled complexes were used in nuclear imaging studies (PET/SPECT).[56-58] The PiB moiety endows the probes with specific affinity towards Aβ aggregates and, by absorbing in the visible spectral window through the conjugated π system, acts as an antenna for sensitizing Ln^{3+} luminescence. The photophysical properties of the antenna have been evaluated in the absence of the metal ions and in the complexes. The luminescence study provides information on structural features such as coordination geometry and metal hydration. The determination of the overall luminescence quantum yield and the overall efficiency of energy transfer are useful to evaluate the optical probe efficiency, and could be correlated with the distance between the antenna and the metal center as determined by DFT computation. Based on the results of this study, future synthetic work should be directed towards optimizing the photophysical properties of the Eu^{3+} complexes.

2. Materials and Methods

2.1. Reagents, general equipment and solutions

The trivalent lanthanide chlorides were obtained from Sigma-Aldrich and deuterium oxide (99.9% D) was obtained from Euriso-top®. The other chemicals were purchased from Sigma-Aldrich and used without further purification. Ligands L1 and L2 were synthesized as previously reported.[54-55] The Ln^{3+} complexes of the two ligands were prepared by mixing solutions of trivalent lanthanide chlorides and the ligand in equimolar quantities and adjusting the pH to 5.5 using aqueous NaOH solutions (10 or 100 mM). The pH measurements were carried out with a Crison micropH 2000 pH meter, coupled to a SemTix Mic pH 014/0 electrode. The solutions were allowed to react for 24 h at 60°C while the pH was regularly controlled. The presence of free metal ion was checked in each sample using the xylenol orange test.[59] This was continued until the test was negative, confirming full Ln^{3+} complexation. The concentrations of the paramagnetic complexes were quantified by the NMR Evans method.[60,61] The ^{1}H NMR spectra were obtained on a Varian VNMRS 600 MHz (14.09 T) spectrometer operating at 600.14 MHz.

2.2. UV-Vis spectrophotometry

The acquisition of the absorption spectra of the L1 and L2 ligands and of their complexes in aqueous solutions, the determination of molar absorption coefficients and the spectrophotometric analysis of the photodegradation of the two ligands were carried out at room temperature using Spectronic Unicam UV500 and Secoman® Uvikon XL UV/Vis spectrophotometers.

2.3. Photodegradation studies

A photodegradation study of the two ligands was undertaken using a Semi-Micro photochemical reactor (Applied Photophysics), in which 10 mM sodium phosphate buffer aqueous solutions (pH= 7.4) of ligands L1 or L2 were placed in a cell with an optical path of 1 cm and irradiated at 350 nm. UV-Vis absorption spectra were registered at different irradiation times.

2.4. Steady-state fluorescence and luminescence measurements

The ligand emission, excitation (collected at the maximum emission wavelength) and lanthanide luminescence spectra were obtained at room temperature with a Cary Eclipse (Varian) fluorescence spectrophotometer using the Varian Cary Eclipse software (version 1.1). The spectra obtained were not corrected for the instrumental response. The emission and excitation spectra at 77 K were recorded on a Fluorog 3.2.2 (Horiba-Jovin-Yvon) fluorimeter and these were corrected for the wavelength response of the system.

The ligand fluorescence quantum yields (ϕ_F) and the overall luminescence quantum yields (ϕ_L^{Ln}) were determined by a comparative method[62] using quinine sulfate (λ_{ex} = 366 nm, ϕ_F = 0.546 in 0.5 M H_2SO_4 degassed solution)[63] and tris(bipyridine)ruthenium(II) chloride ([Rubpy$_3$]Cl$_2$, ϕ =0.02861 in air-equilibrated aqueous solution)[64], respectively. The fluorescence quantum yields were determined using the equation:[65]

$$\phi_F^{\mathrm{cp}} = \frac{\int \mathrm{I}(\lambda)^{\mathrm{cp}}\mathrm{d}\lambda}{\int \mathrm{I}(\lambda)^{ref}\mathrm{d}\lambda} \times \frac{\mathrm{OD}_{\mathrm{ref}}}{\mathrm{OD}_{\mathrm{cp}}} \times \frac{n_{\mathrm{cp}}^2}{n_{\mathrm{ref}}^2} \times \frac{f_{\mathrm{des}}^{\mathrm{cp}}}{f_{\mathrm{des}}^{\mathrm{ref}}} \times \phi_F^{\mathrm{ref}} \qquad (1)$$

where $\int \mathrm{I}(\lambda)^{\mathrm{x}}\,\mathrm{d}\lambda$ is the integrated area under the emission spectra of the sample (cp) and of the reference compound (ref); OD_x are the optical densities of the ref and cp at the excitation wavelength; n_x is the solvent refractive index in which the cp and the ref were dissolved (n_{H_2O} 1.333, n_{D_2O}= 1.328 and $n_{H_2SO_4,\,0.5M}$=1.338)); f_{des}^{x} is the degassing factor, which takes into account the effect of oxygen dissolved in the sample on the fluorescence intensity. Since the ϕ_F values of the compounds were determined using optically matched solutions of the sample and reference compounds, the OD^{cp}/OD^{ref} ratio equals 1. At the excitation wavelength used, the OD was kept between 0.1-0.2 in order to avoid inner filter effects. Additionally, the samples were previously degassed, thus f^{cp}/f^{ref} =1.

The luminescence and luminescence excitation spectra were recorded using the following experimental conditions: number of flashes = 5, delay time = 100 μs, gate time =1 ms, excitation slit = 20 nm, emission slit = 2.5 nm for the Eu^{3+} complexes, emission slit = 5 nm for the Tb^{3+} complexes, increment times = 0.3 nm, averaging time = 0.1 s and a photomultiplier voltage of 800 V for the LnL1 complexes and 950 V for the LnL2 complexes. The luminescence excitation spectra were collected at the maximum emission wavelength (616 nm for the Eu^{3+} complexes and 545 nm for the Tb^{3+} complexes). We found that the emission shutter with the delayed time used was not able to eliminate completely the fluorescence emission. To overcome this, the baseline was corrected.

The measurements of luminescence lifetimes were made in deionized water (H_2O) and deuterium oxide (D_2O). The luminescence decay times were obtained after 10 flashes, with delay time of 100 μs, gate time of 10 μs, excitation slit of 20 nm and emission slit of 10 nm. The photomultiplier voltage was kept at 1000 V and the decay curves were obtained from the average of 100 decays. The excitation was done at the maximum of the absorption spectrum and the emission was monitored at 701 nm for the Eu^{3+} complexes and 587 nm for the Tb^{3+} complexes. The decay curves were fitted with a mono-exponential function, and the luminescence lifetimes were obtained from the average of three independent samples.

2.5. Time-resolved Fluorescence

Picosecond time-resolved fluorescence measurements were performed using a home-built picosecond TCSPC (Time Correlated Single Photon Counting)[66] apparatus. For ligand L1 and respective complexes excitation was made at 339 nm using a picoLED as excitation source. For ligand L2 and respective complexes the excitation source consisted of a picosecond Spectra Physics mode-lock Tsunami laser (Ti: sapphire) model 3950 (repetition rate of about 82 MHz, tuning range 700–1000 nm), pumped by a Millennia Pro-10s, frequency-doubled continuous wave (CW), diode pumped, solid-state laser (λ_{em} = 532 nm). A harmonic generator model GWU-23PS (Spectra-Physics) was used to produce the second and third harmonic from the Ti:sapphire laser exciting beam frequency output. The samples were measured with excitation at 372 nm, and the horizontally polarized output beam from the GWU (second harmonic) was first passed through a ThorLabs depolarizer (WDPOL-A) and subsequently through a Glan-Thompson polarizer (Newport 10GT04) with vertical polarization. Emission at 90° geometry collected at magic angle polarization was detected through a double subtractive Oriel Cornerstone 260 monochromator by a Hamamatsu microchannel plate photomultiplier (R3809U-50). Signal acquisition and data processing were performed employing a Becker & Hickl SPC-630 TCSPC module. The fluorescence decay and instrumental response were performed until a maximum of 5×10^3 counts was reached, using a time scale of 22.3 ps/channel for ligand L1 and respective complexes, and 1.74 ps/channel for the ligand L2 and respective complexes.

2.6. Transient absorption measurements

The experimental setup to obtain triplet state absorption spectra used an Applied Photophysics laser flash photolysis apparatus pumped by the third harmonic (355 nm) of a Nd:YAG laser (Spectra Physics). Transient spectra were obtained by monitoring the optical density change at intervals of 10 nm over the 300-600 nm range and averaging at least 5 decays at each wavelength. First-order kinetics was observed for the decay of the transient absorption, assigned to the lowest triplet state. Excitation was at 355 nm with an unfocused beam. Special care was taken in determining triplet yields to have optically matched dilute solutions (absorbance between 0.2-0.3 in a 10 mm square cell) and low laser energy (2 mJ) to avoid multiphoton and triplet-triplet (T-T) annihilation effects. The samples used were degassed with nitrogen during approximately 20 minutes and sealed.

The triplet-triplet molar absorption coefficients were determined by the singlet depletion technique according to the well-known relationship:[65]

$$\varepsilon_T = \frac{\varepsilon_S \Delta \mathrm{OD}_T}{\Delta \mathrm{OD}_S} \qquad (2)$$

where ΔOD_S and ΔOD_T are the changes in optical density due to singlet depletion and to triplet absorption in the differential transient absorption spectra, respectively, and ε_S is the singlet molar extinction coefficient. The intersystem-crossing yields (ϕ_T) for the compounds were obtained by comparing the ΔOD of the standard (benzophenone in ethanol, $\varepsilon_{TT}^{benzophenone}$ = 7300 M^{-1} at 545 nm) optically matched (at the laser excitation wavelength) and of the compound using the following equation:

$$\phi_T^{\mathrm{cp}} = \frac{\varepsilon_{TT}^{benzophenone}}{\varepsilon_{TT}^{cp}} \times \frac{\Delta OD_{max}^{cp}}{\Delta OD_{max}^{benzophenone}} \times \phi_T^{\mathrm{benzophenone}} \qquad (3)$$

Room-temperature singlet oxygen phosphorescence was detected at 1270 nm with a Hamamatsu R5509-42 photomultiplier cooled to 193 K in a liquid nitrogen chamber (Products for Research model PC176TSCE-005) after laser

excitation at 355 nm in an adapted Applied Photophysics flash kinetic spectrometer. The singlet oxygen formation quantum yield values, ϕ_{Δ}^{cp}, were determined by plotting the initial emission intensity for optically matched solutions as a function of the laser energy and comparing the slope with that obtained upon sensitization with the reference compound (^{1}H–phenalen-1-one in toluene), according to the following equation:

$$\phi_{\Delta}^{cp} = \frac{\text{slope}^{cp}}{\text{slope}^{1H-\text{Phenalen}-1-\text{one}}} \times \phi_{\Delta}^{1H-\text{Phenalen}-1-\text{one}} \qquad (4)$$

where $\phi_{\Delta}^{1H-\text{Phenalen}-1-\text{one}}$ = 0.93, at λ_{exc} = 355 nm.

2.7. Computational study

The structures and energies of six conformers of the $[EuL1(H_2O)]^-$ complex and two conformers of the $[EuL2(H_2O)]$ complex were calculated at the DFT (Density Functional Theory) level of theory within the hybrid meta-GGA approximation with the TPSSh[67] exchange correlation functional and using the GAMESS-US code.[68] The geometries were fully optimized, without symmetry constrains, using the effective core potential (ECP) of Dolg *et al.* and the associated [5s4p3d]-GTO valence basis set for the europium[69] atom and the 6–31G(d,p) standard basis set for sulfur, oxygen, nitrogen, carbon and hydrogen atoms. The ECP of Dolg *et al.* for europium includes the 4f electrons in the core and leaves the 5s and 5p electrons to be treated explicitly. The approximation of attributing the 4f electrons to the core of the ECP is reasoned by the fact that the 4f-orbitals have limited radial extension and therefore have an almost negligible participation in chemical bonding in lanthanide compounds.[70,71] Vibrational frequency calculations were carried out on the resultant stationary points for each conformer to confirm that they are true minima in the potential energy surface (i.e., to confirm that there are no imaginary frequencies). The relative Gibbs energies and equilibrium populations of the different conformers were calculated at 298.15 K.

3. Results and discussion

3.1. Ligand-centered emission

3.1.1. Photophysical properties of the free ligands L1 and L2

The spectral window and the absorption intensity are important features in the design of luminescence probes. *In vivo* excitation should not occur at a wavelength that could destroy cells, thus the probe should absorb above 330 nm.[52] A strong absorption, characterized by the molar absorption coefficient, improves the probe efficiency, which can be enhanced by sensitization of the metal ion through energy transfer from the chromophore.

The photophysical properties of the phenyl-benzothiazole (PiB) moiety in the free ligands were characterized first. The absorption spectra of the free ligands L1 and L2 in aqueous solution show a maximum at wavelengths (λ_{abs}) 330 nm and 360 nm, respectively (Figure S1 and Table 1), in the range adapted for biological applications. This band is assigned to a $\pi\rightarrow\pi^*$ transition in the phenyl-benzothiazole moiety. The red-shift observed in the λ_{abs} of this absorption band from L1 to L2 is due to the presence of substituent groups with different electronic densities in their chemical structure. While L2 has two electron donating substituents (alkoxide and amide groups) at the terminal positions of the phenyl-benzothiazole moiety, L1 has an electron donating group (methoxy) and an electron withdrawing group (amine). This causes a larger energy increase of the ground singlet state (S_0) relative to the first excited state S1 of the chromophore in L2 than in L1, leading to a red-shift of the absorption band due to the decrease of the optical band gap, as observed for other substituted benzothiazoles.[72] Both ligands have high molar absorption coefficients, ε_{abs} = 40500 ± 3300 $M^{-1}cm^{-1}$ for L1 and 28400 ± 350 $M^{-1}cm^{-1}$ for L2 (Table 1). These absorption parameters are not changed in the TbL1 and TbL2 complexes, showing that these parameters of the PiB chromophore are not influenced by the Ln^{3+} complex moiety.

The fluorescence emission spectra of L1 and L2 at room temperature in aqueous solution in a 10 mM sodium phosphate

Table 1 - Photophysical properties of the PiB conjugate ligands (L1 and L2) and of the respective Ln^{3+} complexes (10 mM sodium phosphate buffer, pH= 7.4).[a] The margins of error indicated are at a 95% confidence level.

	L1	LaL1	EuL1	TbL1	L2	LaL2	EuL2	TbL2
λ_{abs} (nm)	330	330	330	330	360	360	360	360
ε_{abs} ($M^{-1}cm^{-1}$)	4.05(± 0.33)×10^4	-	-	4.05(± 0.33)×10^4	2.84(±0.035)×10^4	-	-	2.84(±0.035)×10^4
λ_F (nm)	410	410	410	410	445	445	445	445
λ_T (nm)	460	460	460	460	450	450	450	450
ε_T ($M^{-1}cm^{-1}$)	4.01×10^4	3.90×10^4	3.28×10^4	-	2.6×10^4	-	-	-
ϕ_F (nm)	0.61± 0.02	0.61±0.02	0.49±0.02	0.61±0.02	0.64±0.03	0.62±0.02	0.35±0.02	0.60±0.03
ϕ_T	0.27	0.26	0.24	-	0.15	-	-	-
ϕ_Δ	0.06	0.07	0.07	-	-	-	-	-
ϕ_{IC}	0.12	0.13	0.27	-	0.21	-	-	-
τ_F (ns)	1.80	1.82	τ_1=1.66 (a_1=0.691)* τ_2=0.88 (a_2=0.309)	1.78	1.56	1.49	τ_1=1.18 (a_1=0.664)* τ_2=0.17 (a_2=0.336)	1.49
τ_T (ns)	94	85	68	87	153	152	4.06	121
k_F (ns^{-1})	0.34	0.33	0.30	0.34	0.41	0.42	0.30	0.40
k_{NR} (ns^{-1})	0.22	0.22	0.31	0.22	0.23	0.25	0.55	0.27
k_{IC} (ns^{-1})	0.07	0.07	0.16	-	0.13	-	-	-
k_{ISC} (ns^{-1})	0.15	0.14	0.14	-	0.10	-	-	-

[a] Spectral data: absorption (λ_{abs}) and fluorescence (λ_F) wavelength maxima, triplet–triplet absorption (λ_T) maxima, and molar extinction singlet (ε_{abs}) and triplet (ε_T) coefficients. Photophysical properties: fluorescence quantum yields (ϕ_F), intersystem crossing singlet-to-triplet quantum yields (ϕ_T), quantum yields for singlet oxygen formation (ϕ_Δ), internal conversion quantum yields (ϕ_{IC}), fluorescence lifetimes (τ_F), triplet lifetimes (τ_T), radiative (k_F), radiationless internal conversion (k_{IC}), and intersystem crossing (k_{ISC}) rate constants; $k_F = \phi_F/\tau_F$; $k_{NR} = (1 - \phi_F)/\tau_F$; $k_{IC} = (1 - \phi_F - \phi_T)/\tau_F$; $k_{ISC} = \phi_T/\tau_F$; $\phi_{IC} = 1 - \phi_F - \phi_T$; The fluorescence decay curves were collected at λ_{em} = 410 nm and λ_{em}= 450 nm, for the L1 and L2 ligands and their complexes;
*The EuLi complexes have a bi-exponential fluorescence decay and the pre-exponential factors a_1 and a_2 are indicated in parentheses.

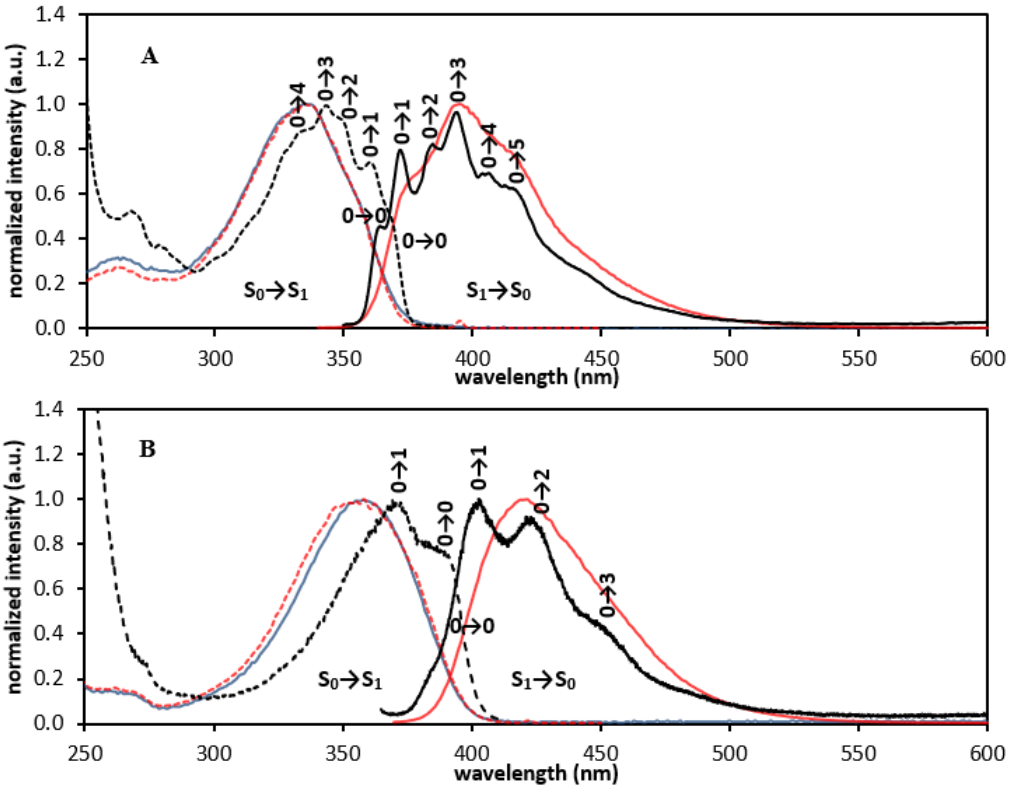

Figure 2. Absorption (blue line), emission (red solid line) and excitation (red dashed line) spectra for L1 (**A**) and L2 (**B**), in ethanol at 298 K. The fluorescence emission (black solid line) and excitation (black dashed line) spectra at 77 K are also presented. For L1 and L2, the fluorescence emission spectra were recorded with excitation at 330 nm and 360 nm, respectively, and for the excitation spectra the fluorescence emission was recorded at 410 nm and 443 nm, respectively.

buffer (pH= 7.4) (Figure S1A) show a non-resolved emission band with maxima at 410 nm and 445 nm, respectively. The ligands display very similar photophysical properties (Table 1): large Stokes shifts (80 nm (5913 cm^{-1}) and 85 nm (5306 cm^{-1}), respectively), high singlet excited state (S1) energies (324.40 (27100) and 294.12 (24570) kJ/mol (cm^{-1}), respectively), high fluorescence quantum yields (ϕ_F = 0.61 and 0.64 for L1 and L2, respectively) and mono-exponential fluorescence decays (τ_F = 1.80 ns and 1.56 ns for L1 and L2, respectively). Decreasing the temperature to 77 K, the emission spectra of L1 and L2 in ethanol display an increase of their vibrational structure (Figure 2), which is the result of the confinement of the ligands into a more rigid environment.

3.1.2. Ligand singlet and triplet excited states in the presence and absence of metal ion

The presence of the Ln^{3+} ion changes the properties of the singlet and triplet excited states of the phenyl-benzothiazole chromophore, which, after excitation, sensitizes the excited state of the metal ion. The triplet state of the ligands, in the absence and presence of bound Ln^{3+}, has been characterized by laser flash photolysis (Table 1). Figure 3 depicts the transient singlet-triplet difference absorption spectra of ligand L1 in a degassed buffer solution. The depletion of the ground-state leads to the disappearance of a band at 330 nm, represented by a negative optical density (O.D.) variation, and the formation of a new band at 460 nm (positive O.D variation), which is assigned to the ligand L1 **triplet state.** Similar spectra were obtained for ligand L2 and in the presence of Ln^{3+} ions. The triplet decay time (τ_T), the intersystem-crossing (ϕ_T) and internal conversion (ϕ_{IC}) quantum yields and the triplet-triplet absorption coefficient (ε_T) are very similar for L1 and LaL1, with small changes observed for EuL1. The presence of Eu^{3+} leads to a decrease of τ_T and an increase of ϕ_{IC}. Comparing L1 and L2, τ_T and ϕ_{IC} increase, whereas ϕ_T and ε_T decrease for the latter ligand. Overall, the photophysical parameters shown in Table 1 indicate that the

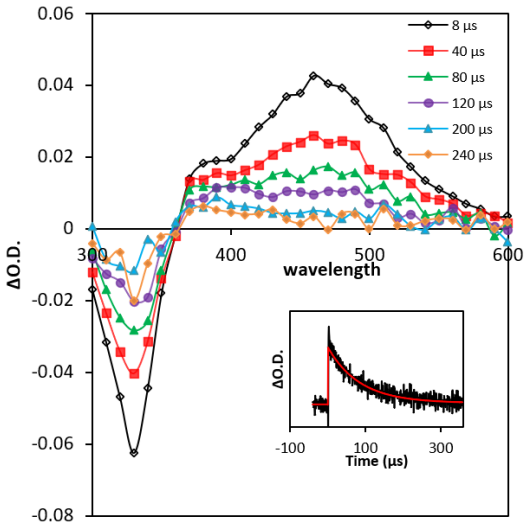

Figure 3. Time resolved transient triplet-singlet absorption difference spectra for the ligand L1 in 10 mM sodium phosphate buffer (pH = 7.4), observed with different delays following laser excitation at 355 nm. The triplet-triplet absorption decay obtained at 450 nm is shown as an inset.

presence of the lanthanide ion does not affect (LaLi, TbLi) or slightly (EuLi) affects the triplet state of the antenna in the L1 and L2 complexes studied.

The luminescence sensitization pathway of the Tb^{3+} and Eu^{3+} complexes occurs in three steps: excitation of the phenyl-benzothiazole moiety (antenna) into its singlet excited state, followed by intersystem crossing yielding the formation of the antenna´s triplet excited state, and finally energy transfer from the triplet state to the lanthanide ion. While we cannot exclude some contribution to the energy transfer from the donor excited singlet state, this is expected to be less important because the singlet state lifetime is markedly shorter than the triplet one. The excited state properties of the phenyl-benzothiazole moiety in the L1 and L2 probes remains unchanged upon La^{3+} complexation, demonstrating that the presence of a non-luminescent metal ion does not influence the photophysical proprieties of the ligand (Table 1). In contrast, in the case of the Eu^{3+} complexes, EuL1 and EuL2, the presence of the cation causes a decrease of the fluorescence quantum yields (ϕ_F), the fluorescence decay times (τ_F) and the triplet lifetimes (τ_T) of L1 and L2 (Table 1). This shows that the excited singlet and triplet states of the antenna are quenched in the Eu^{3+} complexes, in agreement with an efficient energy transfer mechanism from the triplet state of the antenna to the metal center. It should be noted that while the triplet lifetime for EuL2 is markedly shorter than that of the ligand L2, with EuL1, there is only a modest decrease in triplet lifetime relative to that of L1. However, more efficient triplet sensitization is observed with EuL1. A possible explanation for this apparent contradiction is the involvement of some other triplet quenching mechanism, such as charge transfer from the amine group, in EuL2.

Time-resolved fluorescence measurements of the free ligands collected at their maximum emission wavelengths resulted in mono-exponential decays with decay times (τ_F) of 1.80 and 1.56 ns for L1 and L2, respectively, in buffer solution. The same behavior was found for the La^{3+} and Tb^{3+} complexes. Bi-exponential decays were obtained for the EuL1 and EuL2 complexes (Table 1 and Figure S2). The fact that no rise-time was observed indicates that these correspond to two distinct species. A possible explanation is that these are associated with different conformations of the complexes. A representative determination of the rate constants for the SA/TSA conformer interconversions in DOTA-type Ln^{3+} complexes has been carried out by quantitative analysis of variable temperature EXSY NMR spectra of $Yb(DOTA)^-$. It was shown that the arm rotation and ring inversion processes had quite similar activation energies, E_a, in the 65-90 $kJ.mol^{-1}$ range, corresponding to exchange kinetic constants, k_{exch}, at 297 K in the 14.4 – 116.7 s^{-1} range. This reflects the high internal rigidity of the macrocyclic complexes, which explains the observed slow SA/TSA interconversion in the proton NMR timescale. Thus, these processes are too slow to explain the bi-exponential characteristics of the luminescence lifetimes of the EuL1 and EuL2 complexes.[73] An alternative explanation of the bi-exponential decay is by considering an equilibrium of the complex between a fully extended conformation, which is the more stable one according to the DFT study (Table 3 and Figures 5 and 6), originating the component with the longer fluorescence lifetime (Table 1), and a conformation where the chromophore is oriented towards the metal ion, originating the component with shorter fluorescence lifetime. In the case of the EuL2, the fact that it has a longer spacer with high conformational freedom and allowing a closer approximation between the chromophore and the metal ion, would decrease the component with shorter fluorescence lifetime more significantly than in the case of EuL1. These slight conformation changes are expected to be in a timescale that explains the bi-exponential characteristics of the fluorescence lifetime. Otherwise there is little or no effect on that parameter.

3.1.3. Photostability of the ligands

A photostability study of the ligands and their complexes is very important for their evaluation as optical probes. Figure S3 shows that no significant change was observed in the absorption spectrum of ligand L1, following two hours of irradiation using 350 nm light (intensity 90 mW/cm2) in a semimicro photoreactor described in detail elsewhere.[74] The light intensity is comparable with that of the excitation lamp in conventional fluorimeters, demonstrating acceptable photostability. However, under the same conditions, ligand L2 showed a continuous decrease in the intensity of its 360 nm absorption band, with a corresponding shift to shorter λ_{abs} values, indicating that it is photodegradable. Although the photo-degradation mechanism was not studied and photoproducts were not isolated and identified, the presence of two isosbestic points at 240 nm and 325 nm indicates that ligand L2 photoreacts to give one degradation product. The limited photostability of L2, and possibly of its Ln^{3+} complexes, indicates that their usefulness as optical probes is limited.

3.2. Metal-centered emission

3.2.1. Luminescence spectra

Excitation of the ligand-centered $\pi \rightarrow \pi^*$ transitions at the maximum absorption wavelengths, 330 nm and 360 nm, respectively, was used to acquire the emission spectra of the visible-emitting EuLi and TbLi (i = 1, 2) complexes (Figures 4 and S4). All the compounds show characteristic red and green emissions, with emission profiles typical of the Ln^{3+} ion used. Figure 4 shows the luminescence spectra of the EuL1 and EuL2 complexes, with seven emission bands corresponding to transitions from the lowest excited state $^5D_0$ to the different levels of the ground state, ^7F_J ($^5D_0 \rightarrow {}^7F_J$, J = 0 - 6). The asymmetric electronic ligand field destroys the spherical symmetry of the Eu^{3+} ion, splitting each spectroscopic energy level with different quantum number J in several sub-levels, the splitting being dependent on the group point symmetry of the complex. The intensity of some transitions is highly dependent of the chemistry environment and are called “hypersensitive transitions”. From the spectrum we can observe that the $^5D_0 \rightarrow {}^7F_1$, the magnetic dipole transition (which is largely independent of the Eu^{3+} environment), and the $^5D_0 \rightarrow {}^7F_4$ transition have relative intensities similar to the hypersensitive $^5D_0 \rightarrow {}^7F_2$ transition, reflecting similar high-symmetry chemical environments around the Eu^{3+} ion, in agreement with other studies involving complexes of DOTA and DO3A derivatives.[75,76] In fact, although the total symmetry of the complexes is C1, the

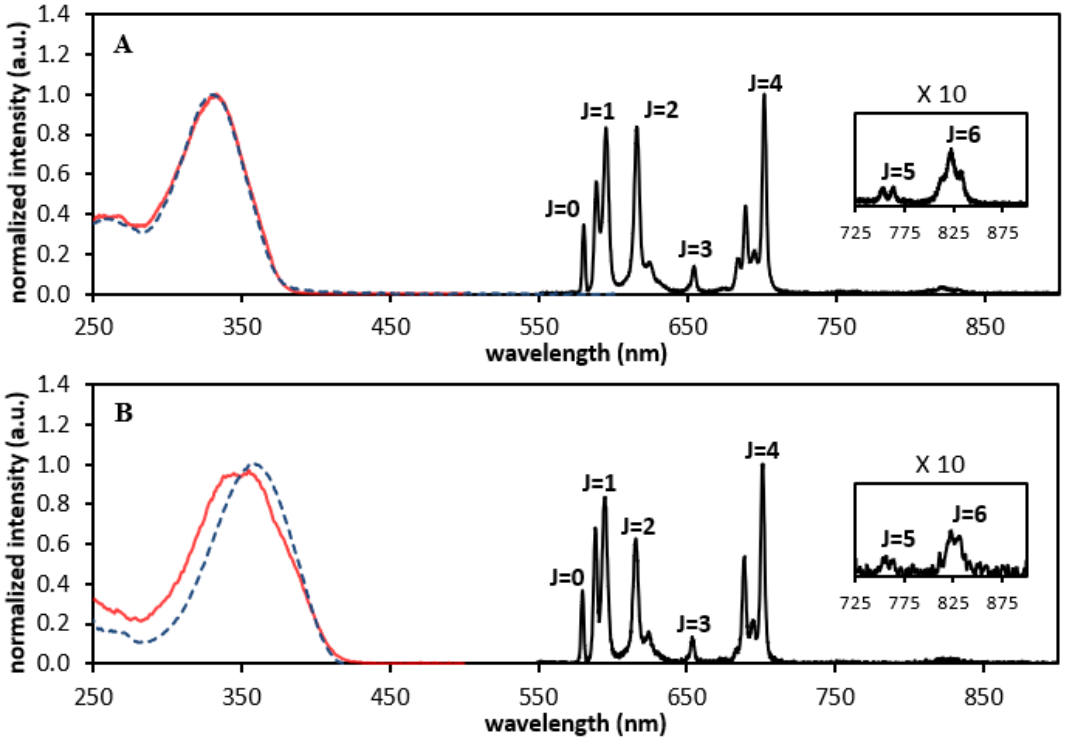

Figure 4. Luminescence spectra (black line) of the EuL1 (**A**) and EuL2 (**B**) complexes in 10 mM sodium phosphate buffer (pH = 7.4), collected with excitation wavelengths of 330 nm and 360 nm, respectively, at T = 298 K. The absorption (blue dashed line) and the luminescence excitation (red line) spectra are also presented. In the luminescence spectra, the J = 0 - 6 levels of the Eu^{3+} ground state involved in the electronic transitions $^5D_0 \rightarrow ^7F_J$ are indicated. The emission for the luminescence excitation spectra was collected at 616 nm.

symmetry of their coordination sphere is close to C4. However, the hypersensitive $^5D_0 \rightarrow ^7F_2$ transition has a considerably higher intensity in the emission spectrum of EuL1 relative to EuL2.

The strongly forbidden electronic dipole $^5D_0 \rightarrow ^7F_0$ transition is allowed in a selected number of symmetries only (C_{nv}, C_n, and C_s).[75,76] Here the transition is detectable as a single symmetric peak at 579.55 nm (17254.77 cm^{-1}) for EuL1 and at 579.85 nm (17245.84 cm^{-1}) for EuL2, constituting 13.23% and 14.19% of the integrated intensity of the magnetic dipole $^5D_0 \rightarrow ^7F_1$ transition for EuL1 and EuL2, respectively. This is an indication of pseudo-C4 symmetry about the Eu^{3+} ion, which is further reflected by the crystal-field splitting of the other $^5D_0 \rightarrow ^7F_J$ transitions. Because the $^7F_0$ states of Eu^{3+} are non-degenerate, no crystal-field fine structure is expected for the $^7F_0 \rightarrow ^5D_0$ line. Thus, the number of bands observed for this transition is a measure of the number of non-equivalent Eu^{3+} species present in solution.[75,76] However, with the rather wide beam width used in our experiments (2.5 nm) it is not possible to comment on the presence of any isomers in solution. Ln^{3+} complexes with DOTA and DO3A derivative ligands can adopt in solution square antiprismatic (SAP) and twisted square antiprismatic (TSAP) geometries, which differ in the value and sign of the torsion angle between the plane defined by the four Ln^{3+}-bound nitrogen atoms of the macrocyclic ring and the plane defined by the four Ln^{3+}-bound oxygens of the pendant arms.[77,78] Based on the luminescence data, we can conclude that one of these geometries is much more stable than the other one. Proton NMR spectra of paramagnetic Ln^{3+} complexes of DOTA monoamides in solution indicate that their SAP geometry is significantly more stable than TSAP,[78] a result that is confirmed for our systems by DFT computational results (see later).

The luminescence spectrum of EuL2 shows a non-resolved band at 442 nm that is not related to the Eu^{3+} emission but has the same features of the emission band of the ligand. The luminescence spectrum was obtained with a delay after flash of 0.1 ms, so that band cannot correspond to a normal fluorescence process, since the fluorescence lifetime of the chromophore is less than 2 ns.

The luminescence excitation spectra of EuLi (i = 1, 2), also shown in Figure 4, are very similar to the respective absorption spectra of the ligand. This good spectral overlap fulfils the conditions for populating the lowest Eu^{3+} excited state through energy transfer from the chromophore. According to Latva´s empirical rules,[79] such an energy transfer is efficient when the energy difference (ΔE_{T1Ln^*}) between the antenna T_1 state and the lowest excited state of the Ln^{3+} ion (Ln = Eu, Tb) is in the 1850-5000 cm^{-1} range, suppressing the triplet state and giving high luminescence quantum yields. Assuming that the energy of T_1 of the chromophore in the EuLi complexes is very close to the reported value for 2-phenyl-benzothiazole in a polar solvent (20870 cm^{-1}),[80] the calculated energy differences relative to the $^5D_0$ state for EuL1 and EuL2 (3615.2 cm^{-1} and 3624.2 cm^{-1}, respectively) are within the appropriate range for an efficient T_1-$^5D_0$ energy transfer. Support for energy transfer comes from the decrease of the triplet lifetimes (τ_T) of the Eu^{3+} complexes. In contrast, the La^{3+} ion, without emissive excited electronic states, cannot quench the T_1 state and does not affect the τ_T value of the chromophore. However, as has been pointed out by one of the referees, energy transfer from the triplet state to the Eu^{3+} $^5D_0$ level is forbidden by both multipole and exchange mechanism selection rules. These are relaxed due to J-mixing effects with the energetically close $^5D_1$ and $^5D_2$ levels, and it is

Table 2 - Calculated values of k_{obs}, q, τ_r, k_R, Φ_{Ln}^{Ln}, η_{sens} and Σk_{nr} for the EuL1 and EuL2 complexes using the experimentally determined quantities τ_{obs} and k_{obs} in H_2O and D_2O, $[I_{tot}/I_{(0,1)}]$ and Φ_L^{Ln}. Some other parameters are also shown for TbL1 and TbL2. All parameters have been determined in 10 mM sodium phosphate buffer (pH = 7.4) at 298 K. The margins of error indicated are at a 95% confidence level.

	EuL1	EuL2	TbL1	TbL2
τ_{obs} (H_2O, ms) [a]	0.583 ± 0.003	0.400 ± 0.011	0.298 ± 0.004	0.079 ± 0.010
τ_{obs} (D_2O, ms) [a]	1.871 ± 0.023	0.857 ± 0.017		
k_{obs} (H_2O, s^{-1}) [b]	1716.26 ± 8.3	2500.39 ± 70.5		
k_{obs} (D_2O, s^{-1}) [b]	534.58 ± 6.5	1166.49 ± 22.6		
q [c]	1.12 ± 0.01	1.30 ± 0.07		
$[I_{tot}/I_{(0,1)}]$, H_2O [d]	3.50	3.27		
τ_r, (H_2O, ms) [e]	8.29	8.88		
k_r, (H_2O, s^{-1}) [f]	120.64	112.61		
ϕ_{Ln}^{Ln}, H_2O [g]	0.0703	0.0450		
ϕ_L^{Ln}, H_2O [h]	$1.84\times10^{-3} \pm 7\times10^{-5}$	$1.27\times10^{-4} \pm 3\times10^{-5}$	$2.62\times10^{-4} \pm 1\times10^{-5}$	$2.09\times10^{-5} \pm 6\times10^{-6}$
η_{sens}, H_2O [i]	0.0261	0.00282		
$\sum_n k_n^{nr}$ (H_2O, s^{-1}) [j]	1594.6	2387.4		

a) Luminescence lifetime monitored at the maximum emission at 701 nm; b) Rate constant of observed decay ($k_{obs} = 1/\tau_{obs}$); c) Number of coordinated water molecules in the inner sphere of the Eu^{3+} ion; d) The same as I_{tot}/I_{MD} which is the relative contribution of the $^5D_0 \rightarrow {}^7F_1$ transition, $I_{(0,1)}$, to the total integrated luminescence emission spectrum, I_{tot}.; e) Radiative lifetime in the absence of non-radiative decay processes; f) Radiative rate constant ($k_r = 1/\tau_r$); g) Intrinsic luminescence quantum yield of the Ln^{3+} ion; h) Experimental overall quantum yield of luminescence determined by comparative method using $[Ru(bpy)_3]Cl_2$ as reference in air-equilibrated solution[61]; i) Overall sensitization efficiency to the excited state of the Ln^{3+} ion; j) Sum of all the rate constants for the non-radiative decay of the excited state of the Ln^{3+} ion.

probable that these are involved in the energy transfer from the ligand triplet state. Detailed discussion of the importance of selection rules in this process is given elsewhere.[81-83]

The luminescence spectrum of TbL1 shows the expected seven bands corresponding to the $^5D_4 \rightarrow {}^7F_J$ (J = 0 - 6) transitions, of which four are intense and the other three (J = 0, 1, 2) are weak. However, it was not possible to detect these later bands for the TbL2 complex (Figure S4). The luminescence spectra of TbL1 and TbL2 also show two bands at 408 nm and 442 nm, respectively, which result from delayed fluorescence of the chromophore. The effect of the Tb^{3+} ion on the reduction of the chromophore triplet lifetimes (τ_T) in the TbLi complexes is much smaller than for the EuLi complexes (Table 1), indicating that the energy transfer from the T_1 state to the $^5D_4$ state of Tb^{3+} is less efficient. This could be explained by the calculated energy differences between those states (ΔE_{T1Tb*}) for TbL1 and TbL2 (366.4 cm^{-1} and 379.5 cm^{-1}, respectively), which are much smaller than 1850 cm^{-1}, a situation that according to Latva´s empirical rules[79] facilitates the $^5D_4 \rightarrow T_1$ back transfer process. The luminescence excitation spectrum of TbL2 is again quite similar to the respective absorption spectrum. However, in the case of TbL1, although the maxima of the two bands coincide in the excitation and absorption spectra, their relative intensities are very different in the two kinds of spectra, suggesting that long-range dipolar Förster resonance energy transfer (FRET) mechanism from the chromophore donor to the metal acceptor is not efficient and there may be a contribution from the short range exchange Dexter mechanism,[65] which is facilitated for donor-acceptor distances below 10 Å.[84] In fact, the average distance between the Tb^{3+} ion and the closest atom (P1) where the LUMO (lowest unoccupied molecular orbital) of the chromophore has a significant charge density in the TbL1 complex is 7.73 Å, as calculated by DFT (see the later discussion). The Förster mechanism should dominate the energy transfer process in the TbL2 complex, for which the Dexter mechanism is highly improbable. This is supported by the large (greater than 10 Å) DFT computed average distance between the chromophore and Tb^{3+}, separated by a saturated aliphatic six carbon chain in a low energy all-trans conformation (see later).

3.2.2. Photophysical properties of the luminescent complexes

The efficiency of the overall sensitization process of the Eu^{3+} and Tb^{3+} complexes was evaluated through the determination of the overall quantum yield of luminescence (ϕ_L^{Ln}), using $[Ru(bpy)_3]Cl_2$ in an air equilibrated aqueous solution as reference.[64] These experimental values (Table 2) show that the sensitization process has quite low efficiency for all complexes, but LnL2 are about one order of magnitude less efficient than the LnL1. In order to rationalize these absolute and relative values, we note that the overall quantum yield of luminescence can be described as follows:

$$\phi_L^{Ln} = \eta_{pop}^{D} \times \eta_{te} \times \phi_{Ln}^{Ln} = \eta_{sens} \times \phi_{Ln}^{Ln};\ \eta_{sens} = \frac{\phi_L^{Ln}}{\phi_{Ln}^{Ln}} \quad (5)$$

where ϕ_L^{Ln} and ϕ_{Ln}^{Ln} are the quantum yields obtained upon excitation through the ligands (L) or direct excitation into the f-levels (Ln) and η_{sens} is the overall sensitization efficiency of the excited level of the Ln^{3+} ion, which is the product of two terms ($\eta_{pop}^{D} \times \eta_{te}$), where η_{pop}^{D} is the efficiency to populate the donor energy level of the antenna responsible for the energy transfer to the excited level of the Ln^{3+} ion after the initial excitation, and η_{te} is the energy transfer efficiency from the donor energy level to the acceptor level of the Ln^{3+}.[48,85,86] η_{sens}

can be calculated from Equation (5) when ϕ_{L}^{Ln} and ϕ_{Ln}^{Ln} are known. The intrinsic luminescence quantum yield (ϕ_{Ln}^{Ln}) can, in principle, be obtained directly from the intensity of the luminescence spectrum and the measurement of the luminescence lifetime, but this method is difficult to apply due to the for the weak Ln^{3+} f-f bands. An alternative is to use the ratio between the observed rate constant (k_{obs}) and the radiative rate constant (k^{rad}):

$$\phi_{Ln}^{Ln} = \frac{k^{rad}}{k_{obs}} = \frac{\tau_{obs}}{\tau^{rad}} \qquad (6)$$

where $k = 1/\tau$, τ_{obs} is the observed lifetime of the Ln^{3+} emitting level and τ^{rad} is the radiative lifetime of this level. k_{obs} is the sum of the rate constants of the different deactivation processes, including the radiative (k_{rad}) and all the non-radiative (k^{nr}) rate constants:

$$k_{obs} = k^{rad} + \sum_{n} k_{n}^{nr} \qquad (7)$$

Thus, ϕ_{Ln}^{Ln} reflects the extent of the non-radiative deactivation processes occurring in the inner- and outer-coordination spheres of the Ln^{3+}, which depends on the energy gap (ΔE) between the emissive excited state and the highest ground state sub-level of the Ln^{3+}. The lower the ΔE value, the more efficient will be the quenching process by the vibrational overtones of the oscillators present in the ligand and solvent molecules.[48,85,86]

In Equation (6) τ_{obs} can be obtained experimentally, and τ^{rad} can be calculated, although this is generally not easy.[48,85] However, Eu^{3+} is a special case, where the $^5D_0 \rightarrow {}^7F_1$ transition has a purely magnetic dipole (MD) character and can be used as an internal reference, leading to a simplified and convenient equation:

$$\frac{1}{\tau^{rad}} = A_{MD,0} \times n^3 \times \left(\frac{I_{tot}}{I_{MD}}\right) \qquad (8)$$

where $A_{MD,0}$ is a constant equal to 14.65 s^{-1}, n is the refractive index of the solution and (I_{tot}/I_{MD}) is the ratio between the integrated area of the emission spectrum corresponding to all the europium transitions $^5D_0 \rightarrow {}^7F_J$ (J=0-6), I_{tot}, and the integrated intensity of the magnetic dipole transition $^5D_0 \rightarrow {}^7F_1$ (I_{MD} or $I_{(0,1)}$).[87]

The experimental overall (ϕ_{L}^{Ln}) and calculated intrinsic (ϕ_{Ln}^{Ln}) quantum yield values for the EuL1 and EuL2 complexes are shown in Table 2, together with other experimental and calculated parameters. The intrinsic luminescence quantum yield (ϕ_{Ln}^{Ln}) is higher for the EuL1 (0.0703) than for the EuL2 (0.0450). This may reflect structural differences, such as rigidity of the complexes. In the same way, the overall sensitization efficiency (η_{sens}) for EuL1 (0.0261) is an order of magnitude higher than for the EuL2 complex (0.00282). The main reason for these low values, and the consequent low quantum yields of luminescence is the large average distance between the antenna and the metal center in both complexes, which is even bigger for EuL2 (see below), explaining the lower ϕ_{L}^{Ln} value found for this complex. In contrast, reported data in the literature shows that, direct coordination of the chromophore to the metal center leads to quantum yields of luminescence and overall sensitization efficiencies that are one or two orders of magnitude higher than the values obtained for EuL1 complex.[84,85,88,89]

3.2.3. Determination of the number of inner-sphere water molecules

The number of water molecules coordinated in the inner sphere of an Ln^{3+} complex (hydration number, q) can be determined from the difference of the luminescence lifetimes of the complex in H_2O and D_2O, based on the isotope effect observed for the non-radiative quenching of the excited state of the metal ion. This quenching process is more efficient for the O-H than for the O-D oscillator, with a consequent shorter lifetime in H_2O. As a consequence, if non-radiative quenching is dominated by this process, the increase of q will proportionally lower the luminescence lifetime, and can be determined from the difference in efficiency of the process in H_2O and D_2O.[90] The phenomenological relationship proposed for Ln^{3+} complexes, taking into account the small effect of the O-H, N-H and C-H oscillators present in the ligand and in the outer sphere solvent molecules on the decay of the excited state of the metal ion, is given in Equation (9):[91]

$$q = A \times (\Delta k_{obs} + B) \qquad (9)$$

where $\Delta k_{obs} = k_{obs}(H_2O) - k_{obs}(D_2O)$, $k_{obs}=1/\tau_{obs}$, and τ_{obs} is the luminescence lifetime of the complex in ms. In the case of Eu^{3+} complexes, A = 1.2 ms and B = -0.25 ms^{-1}.

The q values obtained for EuL1 and EuL2 are 1.12 and 1.30, respectively (Table 2), which are consistent with q = 1 reported for Eu^{3+} complexes with structurally related octadentate polyaminocarboxylate ligands, such as DOTA and DO3A derivatives, where one water molecule is coordinated to the metal center, increasing the total coordination number to 9.[73] The q values for the Tb^{3+} complexes were not determined, but are expected to be very similar to those found for the Eu^{3+} complexes.

3.3. DFT study of the chelate geometry and the antenna-metal center distance

The tetraaza macrocycles L1 and L2, as α-substituted DOTA and DO3A-monoamide derivatives, respectively, can form Ln^{3+} complexes in solution with two types of geometries: SAP and TSAP.[77,78] As described above, the luminescence spectra of the Eu^{3+} and Tb^{3+} complexes show that only one species is present in solution. In order to investigate which geometry is energetically preferred, theoretical calculations at the DFT level of theory were performed for the complexes, EuL1 and EuL2, with one water molecule coordinated in the inner sphere of the metal ion, based on the calculated q values obtained from the luminescence lifetimes in water and in deuterated water. From these calculations, the relative populations of the SAP and TSAP isomers at 298.15 K were estimated for the two complexes. In each complex, in addition to the chelate geometry, the spacer arm conformation has to be considered. In the $[EuL1(H_2O)]^-$

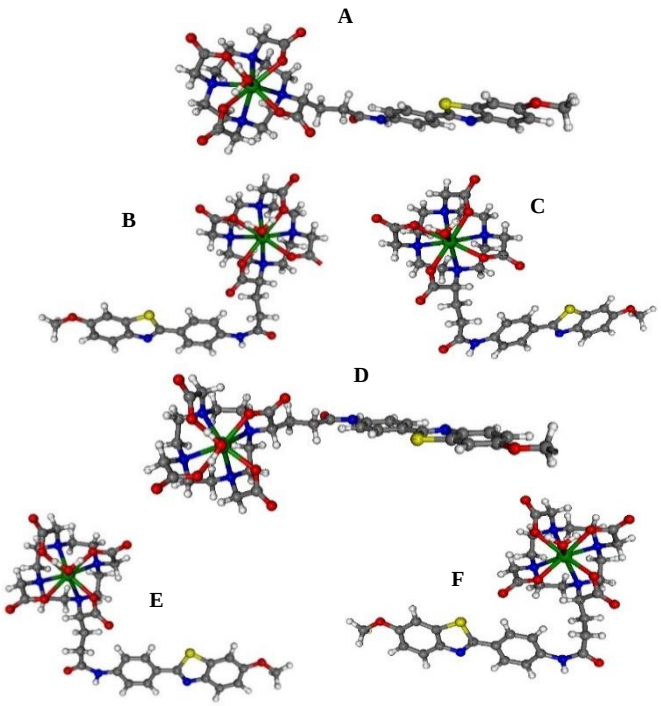

Figure 5. DFT/TPSSh optimized structures of the conformers of the EuL1 complex. The structures **A**, **B** and **C** have SAP geometry and the structures **D**, **E** and **F** have TSAP geometry. The torsional angle C-C-C-N between the portion which binds the PiB moiety and the spacer has the following values in the optimized geometries: 176.0º for **A**, -82.6º for **B**, 76.3º for **C**, 177.1º for **D**, 87.0º for **E** and -80.4º for **F**. Generically, **A** is designated by SAP180, **B** by SAP-90, **C** by SAP+90, **D** by TSAP180, **E** by TSAP+90 and **F** by TSAP-90.

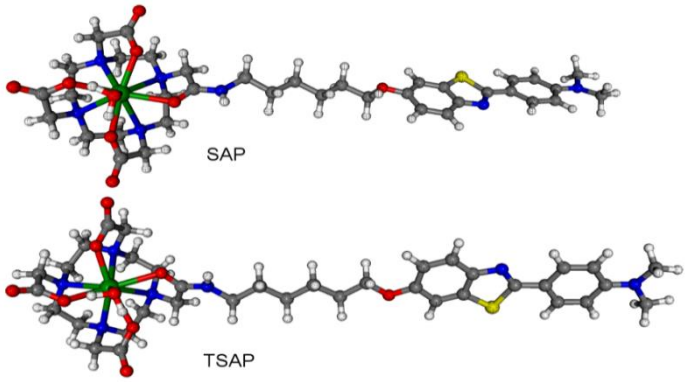

Figure 6. DFT/TPSSh optimized structures of the SAP and TSAP isomers of the $[EuL2(H_2O)]^-$ complex.

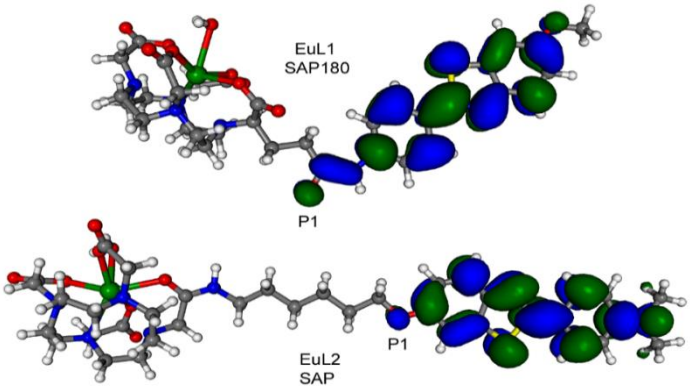

Figure 7. DFT/TPSSh lowest unoccupied molecular orbitals (LUMOs) of the dominant conformers of the EuL1 and EuL2 complexes.

complex, there is torsional flexibility with relatively low steric hindrance for the $H_2C–CN(=O)$ coordinate, describing the torsion angle between the carbon atom of the amide moiety and the adjacent CH_2 group of the spacer arm. However, due to the large size of the complex, it was not possible to carry out a full scan of the energy of the molecule as a function of this coordinate. Therefore, for each type of chelate geometry, we have considered as the most important conformers the structures having C-C-C-N torsional angles (nitrogen atom from the amide and the subsequent three carbon atoms of the spacer) close to 180º, + 90º and -90º. These structures were optimized at the DFT level and their geometries, relative energies and relative populations at 298.15 K are presented in Figure 5 and Table 3. The $[EuL1(H_2O)]^-$ conformers were generically designated as SAP180, SAP+90, SAP-90, TSAP180, TSAP+90 and TSAP-90, combining the indication of their chelate geometry (SAP or TSAP) with that of their approximate C-C-C-N torsional angle (180º, +90º and -90º) (Figure 5).

The theoretical study shows that the most stable conformer for the EuL1 complex is SAP180, adopting an extended conformation of the spacer arm, which has a relative population of 68.3% at 298.15 K. The sum of the populations of all the conformers with SAP geometry is 90.5% (Table 3). Despite the fact that we are not including in this study all the possible minor conformers, this result demonstrates that the SAP geometry is significantly more stable than the TSAP one. This result is consistent with the observation of only one $^5D_0 \rightarrow {}^7F_0$ transition in the luminescence spectrum, showing that only one chelate geometry is detected in solution. This result is also in agreement with proton NMR and X-ray crystal studies from the literature, according to which the Eu^{3+} complexes of DOTA and its α-substituted derivatives generally adopt the SAP geometry in solution with q =1.[77,78]

In the case of the $[EuL2(H_2O)]^-$ complex, the geometry and energy of the SAP and TSAP isomers were calculated with an all-trans conformation of the spacer arm, which is expected as the dominant conformation for the carbon chain, since in this extended conformation the steric effects are minimized. The theoretically optimized geometries of the isomers are presented in Figure 6. This study shows that the SAP isomer is again the most stable form, being 1.8 kJ/mol lower in energy than the TSAP one (Table 3). In terms of population at 298.15 K, this corresponds to a population of 67.5% for the SAP geometry and a population of 32.5 % for the TSAP one.

The distance between the metal center and the antenna chromophore is important to ensure high efficiency of energy transfer, and, consequently, a high quantum yield of luminescence. Therefore, this distance (d) was also determined for each of the selected conformations of the Eu^{3+} complexes, either by considering the closest atom (P1) where the LUMO (lowest unoccupied molecular orbital) of the chromophore has a significant charge density, or the centroid of the LUMO orbital (Figure 7). The P1 atom is the oxygen atom of the amide linker in L1 and of the PiB moiety in L2. Table 3 shows that the

Table 3- Relative Gibbs free energies, $\Delta G_{298.15}$ (kJ/mol), equilibrium populations at 298.15 K, $P_{298.15}$ (%) and distances d (Å) between the chromophore (antenna) and the metal center for the isomers of the $[EuL1(H_2O)]^-$ and $[EuL2(H_2O)]^-$ complexes (Figures 5 and 6) calculated at the DFT/TPSSh level of theory.

	EuL1						EuL2	
Conformer	**SAP180**	**SAP-90**	**SAP+90**	**TSAP180**	**TSAP-90**	**TSAP+90**	**SAP**	**TSAP**
$\Delta G_{298.15}$	0.0	2.8	19.7	6.1	18.7	8.7	0.0	1.8
$P_{298.15}$	68.3	22.2	0.0	5.8	0.0	3.6	67.5	32.5
d(Ln-P1)[a]	7.65	8.02	7.93	7.64	8.03	7.74	13.22	13.22
d(Ln-centroid)[b]	10.66	9.01	9.66	10.29	7.86	9.69	19.07	19.02

[a] Distance between the Eu^{3+} ion and the closest atom (P1) of the chromophore (where the LUMO orbital is localized); [b] Distance between the Eu^{3+} ion and the centroid of the LUMO orbital.

calculated distances for the EuL1 conformers (7.64 to 10.66 Å) are considerably smaller than those for EuL2 (13.22 to 19.07 Å) (the same is true if we consider the average distances over all conformers). The efficiency of energy transfer between the triplet state of the chromophore and the Eu^{3+} excited state

decays with their distance, but in different ways depending on the transfer mechanism. In the Förster mechanism the energy transfer decays proportionally to d^{-6}, and in the Dexter mechanism the decay is exponential (e^{-d}).[65] Therefore, both of the mechanisms are in agreement with the observation that EuL1 has a higher luminescence quantum yield than the EuL2 complex. With the determination of the average distance between the antenna and the metal center we can speculate about the nature of the energy transfer mechanism in these complexes. For the occurrence of the short-range Dexter mechanism, which requires an orbital overlap between the donor and acceptor moieties through which an excited electron is transferred, this distance needs to be less than 10 Å.[84] Thus, the average distance calculated for EuL1 is compatible with a contribution of both mechanisms, but the considerably higher than 10 Å average value for EuL2 makes a contribution from the Dexter mechanism to be highly unlikely.

4. Conclusions

The conjugation of the DOTAGA and DO3A chelate to the PiB moiety, which is well known for its high and specific affinity to amyloid aggregates, provided Eu^{3+} and Tb^{3+} complexes with luminescence properties which, according to previous reports, have high affinity to such aggregated amyloid peptides *in vitro*.[36-38,54] The corresponding Gd^{3+} complexes were found to be effective relaxation agents *in vitro*.[36,37,54] Some of their $^{68}Ga^{3+}$ complexes have been studied as PET probes with very limited brain uptake in *in vivo* Alzheimer's disease (AD) animal models,[26] but functionalized multi-walled carbon nanotubes (f-MWNTs) with the $^{111}In^{3+}$ chelates of L1 and L2 were found by SPECT to have enhanced brain delivery in *in vivo* animals.[55] The utility of Eu^{3+} complexes of such PiB conjugates as optical probes has been demonstrated by *ex vivo* immunohistochemical studies using the fluorescence detection of EuDO3A-PiB, which showed that they selectively target Aβ plaques on AD human brain tissue.[36] In this paper we have used luminescence and DFT computational calculations to demonstrate that these probes can be useful luminescence probes for optical imaging, allowing the exploitation of the ligands in multimodality approaches. The PiB amyloid targeting moiety can be used as an antenna to sensitize the lowest excited level of the luminescent Eu^{3+} or Tb^{3+} ion. However, the presence

of one water molecule in the inner coordination sphere of the Ln^{3+}, which provides an efficient relaxation mechanism for the Gd^{3+} complexes in the context of MRI applications, limits the luminescence quantum yield of the corresponding Eu^{3+} (Tb^{3+}) complexes by increasing the number of non-radiative decay routes. The distance between the antenna and the metal center is also a key factor in the development of these probes. While shorter distances increase the quantum yield of luminescence, they lower their affinity to the amyloid aggregates, due to the predominantly hydrophobic nature of their interaction. The low overall quantum yields of luminescence of the Eu^{3+} complexes are mainly due to the low overall sensitization efficiency of their energy transfer process resulting from the large distances between the metal center and the antenna, especially in the EuL2 complex. In overall, the results of this work contribute to the mechanistic understanding of the functioning of such probes and illustrate the challenges associated to the rational design of amyloid multimodal targeted probes.

Conflicts of interest

There are no conflicts to declare.

Acknowledgements

The authors are grateful to the Fundação para a Ciência e a Tecnologia (FCT) for funding of the Coimbra Chemistry Centre through the programmes UIDB/00313/2020 and UIDP/00313/2020, also co-funded by FEDER/COMPETE 2020-EU. TC thanks the Coimbra Chemistry Centre for the award of a research grant from the Project 2015/2020 UID/QUI/00313/2013. ACO thanks the FCT for the PhD grant SFRH/BD/120934/2016. ET and JFM acknowledge financial support of the French ANR (DIVA, ANR-16-CE18-0022-01). We

also thank one of the reviewers for valuable comments on the antenna-lanthanide energy transfer process.

Notes and references

1 M. B. Graeber, S. Kösel, R. Egensperger, R. B. Banati, U. Müller, K. Bise, P. Hoff, H. J. Möller, K. Fujisawa and P. Mehraein, Rediscovery of the case described by Alois Alzheimer in 1911: Historical, histological and molecular genetic analysis, *Neurogenetics*, 1997, **1**, 73.

2 G. Macchi, C. Brahe and M. Pomponi, Alois Alzheimer and Gaetano Perusini: should man divide what fate united? *Behav. Neurol.*, 1997, **4**, 210.

3 D. Galimberti and E. Scarpini, Progress in Alzheimer's Disease, *J. Neurol.*, 2012, **259**, 201.

4 J. A. Hardy and G. A. Higgins, Alzheimer's disease: the amyloid cascade hypothesis, *Science*, 1992, **256**, 184.

5 R. Roychaudhuri, M. Yang, M. M. Hoshi and D. B. Teplow, Amyloid beta-protein assembly and Alzheimer disease, *J. Biol. Chem.*, 2009, **284**, 4749.

6 J. Hardy and D. J. Selkoe, The Amyloid hypothesis of Alzheimer's disease: progress and problems on the road to therapeutics, *Science*, 2002, **297**, 353.

7 K. Rajasekhar, M. Chakrabarti, T. Govindaraju, Function and toxicity of amyloid beta and recent therapeutic interventions targeting amyloid beta in Alzheimer's disease, *Chem. Commun.*, 2015, **51**, 13434.

8 R. Sherrington, E. I. Rogaev, Y. Liang, E. A. Rogaeva, G. Levesque, M. Ikeda, H. Chi, C. Lin, G. Li, K. Holman, T. Tsuda, L. Mar, J. F. Foncin, A. C. Bruni, M. P. Montesi, S. Sorbi, I. Rainero, L. Pinessi, L. Nee, I. Chumakov, D. Pollen, A. Brookes, P. Sanseau, R. J. Polinsky, W. Wasco, H. A. R. Da Silva, J. L. Haines, M. A. Perkicak-Vance, R. E. Tanzi, A. D. Roses, P. E. Fraser, J. M. Rommens, P. H. George- Hyslop, Cloning of a gene bearing missense mutations in early-onset familial Alzheimer's disease, *Nature*, 1995, **375**, 754.

9 E. Levy-Lahad, W. Wasco, P. Poorkaj, D. M. Romano, J. Oshima, W. H. Pettingell, C. Yu, P. D. Jondro, S. D. Schmidt, K. Wang, A. C. Crowley, Y. Fu, S. Y. Guenette, D. Galas, E. Nemens, E. M. Wijsman, T. D. Bird, G. D. Schellenberg, R. E. Tanzi, Candidate gene for the chromosome 1 familial Alzheimer's disease locus, *Science*, 1995, **269**, 973.

10 B. Dubois, H. H. Feldman, C. Jacova, S. T. Dekosky, P. Barberger-Gateau, J. Cummings, A. Delacourte, D. Galasko, S. Gauthier, G. Jicha, K. Meguro, J. O'brien, F. Pasquier, P. Robert, M. Rossor, S. Salloway, Y. Stern, P. J. Visser, P. Scheltens, Research criteria for the diagnosis of Alzheimer's disease: revising the NINCDS-ADRDA criteria, *Lancet Neurol.*, 2007, **6**, 734.

11 W. M. Pardridge, The blood-brain barrier: bottleneck in brain drug development, *NeuroRx.*, 2005, **2**, 3.

12 C. A. Lipinski, Lead-and drug-like compounds: the rule-of-five revolution, *Drug Discov. Today Technol.*, 2004, **1**, 337.

13 D. Balériaux, C. Colosimo, J. Ruscalleda, M. Korves, G. Schneider, K. Bohndorf, G. Bongartz, M. A. Buchem, M. Reiser, K. Sartor, M. W. Bourne, P. M. Parizel, G. R. Cherryman, I. Salerio, L. A. Noce, G. Pirovano, M. A. Kirchin, A. Spinazzi, Magnetic resonance imaging of metastatic disease to the brain with gadobenate dimeglumine, *Neuroradiology*, 2002, **44**, 191.

14 A. Petiet, M. Dhenain, Improvement of microscopic MR imaging of amyloid plaques with targeting and non-targeting contrast agents, *Curr. Med. Imaging Rev.*, 2011, **7**, 8.

15 C. A. Mathis, B. J. Bacskai, S. T. Kajdasz, M. E. McLellan, M. P. Frosch, B. T. Hyman, D. P. Holt, Y. Wang, G.-F. Huang, M. L. Debnath, W. E. Klunk, A lipophilic thioflavin-T derivative for positron emission tomography (PET) imaging of amyloid in brain, *Bioorg. Med. Chem. Lett.*, 2002, **12**, 295.

16 M.-P. Kung, C. Hou, Z.-P. Zhuang, D. Skovronsky, H. F. Kung, Binding of two potential imaging agents targeting amyloid plaques in postmortem brain tissues of patients with Alzheimer's disease, *Brain Res.*, 2004, **1025**, 98.

17 R. Vandenberghe, K. Van Laere, A. Ivanoiu, E. Salmon, C. Bastin, E. Triau, S. Hasselbalch, I. Law, A. Andersen, A. Korner, L. Minthon, G. Garraux, N. Nelissen, G. Bormans, C. Buckley, R. Owenius, L. Thurfjell, G. Farrar, D. J. Brooks, 18F-flutemetamol amyloid imaging in Alzheimer disease and mild cognitive impairment: A phase 2 trial, *Ann. Neurol.*, 2010, **68**, 319.

18 C. M. Clark, J. A. Schneider, B. J. Bedell, T. G. Beach, W. B. Bilker, M. A. Mintun, M. J. Pontecorvo, F. Hefti, A. P. Carpenter, M. L. Flitter, M. J. Krautkramer, H. F. Kung, R. E. Coleman, P. M. Doraiswamy, A. S. Fleisher, M. N. Sabbagh, C. H. Adowsky, E. M. Reiman, S. P. Zehntner, D. M. Skovronsky, Use of florbetapir-PET for imaging β-amyloid pathology, *J. Am. Med. Assoc.*, 2011, **305**, 275.

19 E. Liu, M. E. Schmidt, R. Margolin, R. Koeppe, N. S. Mason, W. E. Klunk, C. A. Mathis, S. Salloway, N. C. Fox, D. L. Hill, A. S. Les, P. Collins, K. M. Gregg, J. Di, Y. Lu, I. C. Tudor, B. T. Wyman, K. Booth, E. Yuen, H. R. Brashear, Amyloid-β 11C-PiB-PET imaging results from 2 randomized bapineuzumab phase 3 AD trials, *Neurology*, 2015, **85**, 692.

20 W. E. Klunk, C. A. Mathis, The future of amyloid-beta imaging: a tale of radionuclides and tracer proliferation, *Curr. Opin. Neurol.*, 2008, **21**, 683–687.

21 S. M. Landau, C. Breault, A. D. Joshi, M. Pontecorvo, C. A. Mathis, W. J. Jagust, M. A. Mintun, Amyloid-β imaging with Pittsburgh compound B and florbetapir: comparing radiotracers and quantification methods, *J. Nucl. Med.*, 2013, **54**, 70.

22 H. Watanabe, M. Ono, S. Iikuni, M. Yoshimura, K. Matsumura, H. Kimura, H. Saji, A (68)Ga complex based on benzofuran scaffold for the detection of β-amyloid plaques, *Bioorganic & Med. Chem. Lett.*, 2014, **24**, 4834.

23 S. Lacerda, J.-F. Morfin, C. F. G. C. Geraldes, É. Tóth, Metal complexes for multimodal imaging of misfolded protein-related diseases, *Dalton Trans.*, 2017, **46**, 14461.

24 K. Chauhan, A. Datta, A. Adhikari, K. Chuttani, A. K. Singh, A. K. Mishra, 68Ga based probe for Alzheimer's disease: synthesis and preclinical evaluation of homodimeric chalcone in β-amyloid imaging, *Org. Biomol. Chem.*, 2014, **12**, 7328.

25 M. Asti, E. Ferrari, S. Croci, G. Atti, S. Rubagotti, M. Iori, P. C. Capponi, A. Zerbini, M. Saladini, A. Versari, Synthesis and characterization of 68Ga-labeled curcumin and curcuminoid complexes as potential radiotracers for imaging of cancer and Alzheimer's disease, *Inorg. Chem.*, 2014, **53**, 4922.

26 D. Cressier, M. Dhilly, T. T. Cao Pham, F. Fillesoye, F. Gourand, A. Maïza, A. F. Martins, J.-F. Morfin, C. F. G. C. Geraldes, É. Tóth, L. Barré, Gallium-68 complexes conjugated to Pittsburgh compound B: radiolabeling and biological evaluation, *Mol. Imaging Biol.*, 2016, **18**, 334.

27 D. J. Hayne, S. Lim, P. S. Donnelly, Metal complexes designed to bind to amyloid-β for the diagnosis and treatment of Alzheimer's disease, *Chem. Soc. Rev.*, 2014, **43**, 6701.

28 A. Forsberg, H. Engler, O. Almkvist, G. Blomquist, G. Hagman, A. Wall, A. Ringheim, B. Långström, A. Nordberg, PET imaging of amyloid deposition in patients with mild cognitive impairment, *Neurobiol. Aging*, 2008, **29**, 1456.

29 X. Chen, P. Yu, L. Zhang, B. Liu, Synthesis and biological evaluation of 99mTc,Re-monoamine-monoamide conjugated to 2-(4-aminophenyl)benzothiazole as potential probes for β-amyloid plaques in the brain, *Bioorg. Med. Chem. Lett.*, 2008, **18**, 1442.

30 Z.-P. Zhuang, M.-P. Kung, C. Hou, K. Ploessl, H. F. Kung, Biphenyls labeled with technetium 99m for imaging beta-amyloid plaques in the brain, *Nucl. Med. Biol.*, 2005, **32**, 171.

31 M. Ono, R. Ikeoka, H. Watanabe, H. Kimura, T. Fuchigami, M. Haratake, H. Saji, M. Nakayama, Synthesis and evaluation of novel chalcone derivatives with (99m)Tc/Re complexes as potential probes for detection of β-amyloid plaques, *ACS Chem. Neurosci.*, 2010, **1**, 598.

32 J. F. Poduslo, G. L. Curran, J. A. Peterson, D. J. McCormick, A. H. Fauq, M. A. Khan, T. M. Wengenack, Design and chemical synthesis of a Magnetic Resonance contrast agent with enhanced in vitro binding, high blood-brain barrier permeability, and in vivo targeting to Alzheimer's disease amyloid plaques, *Biochemistry*, 2004, **43**, 6064.

33 Detection of Alzheimer's amyloid in transgenic mice using Magnetic Resonance Microimaging, Y. Z. Wadghiri, E. M. Sigurdsson, M. Sadowski, J. I. Elliott, Y. Li, H. Scholtzova, C. Y. Tang, G. Aguinaldo, M. Pappolla, K. Duff, T. Wisniewski, D. H. Turnbull, *Magn. Reson. Med.*, 2003, **50**, 293.

34 J. F. Poduslo, T. M. Wengenack, G. L. Curran, T. Wisniewski, E. M. Sigurdsson, S. I. Macura, B. J. Borowski, C. R. Jack, Molecular targeting of Alzheimer's amyloid plaques for contrast-enhanced Magnetic Resonance Imaging, *Neurobiol. Dis.*, 2002, **11**, 315.

35 J. Yang, Y. Z. Wadghiri, D. M. Hoang, W. Tsui, Y. Sun, E. Chung, Y. Li, A. Wang, M. de Leon, T. Wisniewski, Detection of amyloid plaques targeted by USPIO-Aβ1-42 in Alzheimer's disease transgenic mice using Magnetic Resonance Microimaging, *Neuroimage*, 2011, **55**, 1600.

36 A. F. Martins, J.-F. Morfin, A. Kubíčková, V. Kubíček, F. Buron, F. Suzenet, M. Salerno, A. N. Lazar, C. Duyckaerts, N. Arlicot, D. Guilloteau, C. F. G. C. Geraldes, E. Tóth, PiB-conjugated, metal-based imaging probes: multimodal approaches for the visualization of β-amyloid plaques, *ACS Med. Chem. Lett.*, 2013, **4**, 436.

37 A. F. Martins, J.-F. Morfin, C. F. G. C. Geraldes, E. Tóth, Gd3+ complexes conjugated to Pittsburgh compound B: potential MRI markers of b-amyloid plaques, *J. Biol. Inorg. Chem.*, 2014, **19**, 281.

38 A. F. Martins, D. M. Dias, J.-F. Morfin, S. Lacerda, D. V. Laurents, É. Tóth, C. F. G. C. Geraldes, Interaction of PiB-derivative metal complexes with beta-amyloid peptides: selective recognition of the aggregated forms, *Chem. Eur. J.*, 2015, **21**, 5413.

39 G. Bort, S. Catoen, H. Borderies, A. Kebsi, S. Ballet, G. Louin, M. Port, C. Ferroud, Gadolinium-based contrast agents targeted to amyloid aggregates for the early diagnosis of Alzheimer's disease by MRI, *Eur. J. Med. Chem.*, 2014, **87**, 843.

40 W. E. Klunk, M. L. Debnath, J. W. Pettegrew, Chrysamine-G binding to Alzheimer and control brain: Autopsy study of a new amyloid probe, *Neurobiol. Aging*, 1995, **16**, 541.

41 C. Zhu, L. Liu, Q. Yang, F. Lv, S. Wang, Water-soluble conjugated polymers for imaging, diagnosis, and therapy, *Chem. Rev.*, 2012, **112**, 4687.

42 C. J. Sigurdson, K. P. R. Nilsson, S. Hornemann, G. Manco, M. Polymenidou, P. Schwarz, M. Leclerc, P. Hammarstro, K. Wüthrich, A. Aguzzi, Prion strain discrimination using luminescent conjugated polymers, *Nat. Methods*, 2007, **4**, 1023.

43 E. E. Nesterov, J. Skoch, B. T. Hyman, W. E. Klunk, B. J. Bacskai, T. M. Swager, In vivo optical imaging of amyloid aggregates in brain: design of fluorescent markers, *Angew. Chem. Int. Ed.*, 2005, **44**, 5452.

44 A. Åslund, C. J. Sigurdson, T. Klingstedt, S. Grathwohl, T. Bolmont, D. L. Dickstein, E. Glimsdal, S. Prokop, M. Lindgren, P. Konradsson, D. M. Holtzman, P. R. Hof, F. L. Heppner, S. Gandy, M. Jucker, A. Aguzzi, P. Hammarstro, K. P. R. Nilsson, Novel pentameric thiophene derivatives for in vitro and in vivo optical imaging of a plethora of protein aggregates in cerebral amyloidoses, *ACS Chem. Biol.*, 2009, **4**, 673.

45 L. Civitelli, L. Sandin, E. Nelson, S. I. Khattak, A.-C. Brorsson, K. Kågedal, The luminescent oligothiophene p-FTAA converts toxic Aβ1–42 species into nontoxic amyloid fibers with altered properties, *J. Biol. Chem.*, 2016, **291**, 9233.

46 N. P. Cook, V. Torres, D. Jain, A. A. Martí, Sensing amyloid-β aggregation using luminescent dipyridophenazine ruthenium(II) complexes, *J. Am. Chem. Soc.*, 2011, **133**, 11121.

47 J.-C. G. Bünzli, S. V. Eliseeva, Intriguing aspects of lanthanide luminescence, *Chem. Sci.*, 2013, **4**, 1939.

48 J.-C. G. Bünzli, Lanthanide luminescence for biomedical analyses and imaging, *Chem. Rev.*, 2010, **110**, 2729.

49 D. Parker, Luminescent lanthanide sensors for pH, pO2 and selected anions, *Coord. Chem. Rev.*, 2000, **205**, 109.

50 H. Uh, S. Petoud, Novel antennae for the sensitization of near infrared luminescent lanthanide cations, *C. R. Chim.*, 2010, **13**, 668.

51 S. Faulkner, S. J. A. Pope, B. P. Burton-Pye, Lanthanide complexes for luminescence imaging applications, *Appl. Spectrosc. Rev.*, 2005, **40**, 1.

52 A. M. Smith, M. C. Mancini, S. Nie, Bioimaging: Second window for in vivo imaging, *Nat. Nanotechnol.*, 2009, **4**, 710.

53 I. Hemmilä, V. Laitala, Progress in lanthanides as luminescent probes, *J. Fluoresc.*, 2005, **15**, 529.

54 A. F. Martins, A. C. Oliveira, J.-F. Morfin, D. V. Laurents, É. Tóth, C. F. G. C. Geraldes, Associating a negatively charged GdDOTA-derivative to the Pittsburgh compound B for targeting Aβ amyloid aggregates, *J. Biol. Inorg. Chem.*, 2016, **21**, 83.

55 P. M. Costa, J. T.-W. Wang, J. F. Morfin, T. Khanum, W. To, J. Sosabowski, É. Tóth, K. T. Al-Jamal, Functionalised carbon nanotubes enhance brain delivery of amyloid-targeting Pittsburgh compound B (PiB)-derived ligands, *Nanotheranostics*, 2018, **2**, 168.

56 A.D. Sherry, R.D. Brown, III, C.F.G.C. Geraldes, S.H. Koenig, K.-T. Kuan, M. Spiller, Synthesis and characterization of the gadolinium(3+) complex of DOTA-propylamide: a model DOTA-protein conjugate, *Inorg. Chem.*, 1989, **620**, 1989.

57 J.P. André, E. Brücher, R. Kiraly, R.A. Carvalho, H. Mäcke, C.F.G.C. Geraldes, DOTASA, an asymmetrical derivative of DOTA substituted at one acetate pendant arm: ^{1}H NMR and potentiometric studies of the ligand and its lanthanide(III) complexes, *Helv. Chim. Acta*, 2005, **88**, 633.

58 E. Brücher, G. Tircsó, Z. Baranyai, Z. Kovács, A.D. Sherry, in *The Chemistry of Contrast Agents in Medical Magnetic Resonance Imaging*, Ed. A. Merbach, L. Helm, É. Tóth, Eds., Chapter 4, 157, Wiley, Chichester, U.K., 2013.

59 A. Barge, G. Cravotto, E. Gianolio, F. Fedeli, How to determine free Gd and free ligand in solution of Gd chelates. A technical note, *Contrast Med. Mol. Imaging*, 2006, **1**, 184.

60 D. F. Evans, The determination of the paramagnetic susceptibility of substances in solution by nuclear magnetic resonance, *J. Chem. Soc.*, 1959, 2003.

61 D. M. Corsi, C. Platas-Iglesias, H. Van Bekkum, J. A. Peters, Determination of paramagnetic lanthanide(III) concentrations from bulk magnetic susceptibility shifts in NMR spectra, *Magn. Reson. Chem.*, 2001, **39**, 723.

62 J. N. Demas, G. A. Crosby, The measurement of photoluminescence quantum yields. A review, *J. Phys. Chem.*, 1971, **75**, 991.

63 W. H. Melhuish, Quantum efficiencies of fluorescence of organic substances: effect of solvent and concentration of the fluorescent solute, *J. Phys. Chem.*, 1961, **65**, 229.

64 K. Nakamaru, Synthesis, luminescence quantum yields, and lifetimes of trischelated ruthenium(II) mixed-ligand complexes including 3,3′-dimethyl-2,2′-bipyridyl, Bull. *Chem. Soc. Jpn.*, 1982, **55**, 2697.

65 J. S. de Melo, J. Pina, F. B. Dias, A. L. Maçanita, in *Applied Photochemistry*, R. C. Evans, P. Douglas, H. D. Burrows, Eds, Chapter 15, 533, Springer, 2013.

66 J. Pina, J. S. de Melo, H. D. Burrows, A. L. Maçanita, F. Galbrecht, T. Bünnagel, U. Scherf, Alternating binaphthyl−thiophene copolymers: synthesis, spectroscopy, and photophysics and their relevance to the question of energy migration versus conformational relaxation, *Macromolecules*, 2009, **42**, 1710.

67 J. Tao, J. P. Perdew, V. N. Staroverov, G. E. Scuseria, Climbing the density functional ladder: nonempirical meta-generalized gradient approximation designed for molecules and solids, *Phys. Rev. Lett.*, 2003, **91**, 146401.

68 M. W. Schmidt, K. K. Baldridge, J. A. Boatz, S. T. Elbert, M. S. Gordon, J. H. Jensen, S. Koseki, N. Matsunaga, K. A. Nguyen, S. Su, T. L. Windus, M. Dupuis, J. A. Montgomery, General atomic and molecular electronic structure system, *J. Comput. Chem.*, 1993, **14**, 1347.

69 M. Dolg, H. Stoll, A. Savin, H. Preuss, Energy-adjusted pseudopotentials for the rare earth elements, *Theor. Chim. Acta*, 1989, **75**, 173.

70 M. Dolg, H. Stoll, H. Preuss, A combination of quasi-relativistic pseudopotential and ligand field calculations for lanthanoid compounds, *Theor. Chim. Acta*, 1993, **85**, 441.

71 A. F. Martins, S. V. Eliseeva, H. F. Carvalho, J. M. C. Teixeira, C. T. B. Paula, P. Hermann, C. Platas-Iglesias, S. Petoud, E. Tóth, C. F. G. C. Geraldes, A bis(pyridine N -oxide) analogue of DOTA: relaxometric properties of the Gd^{III} complex and efficient sensitization of visible and NIR-emitting lanthanide(III) cations including Pr^{III} and Ho^{III}, *Chem. Eur. J.*, 2014, **20**, 14834.

72 F. Lu, R. Hu, S. Wang, X. Guo, G. Yang, Luminescent properties of benzothiazole derivatives and their application in white light emission, *RSC Adv.*, 2017, **7**, 4196.

73 V. Jacques, J.F. Desreux, Quantitative two-dimensional EXSY spectroscopy and dynamic behavior of a paramagnetic lanthanide macrocyclic chelate: YbDOTA (DOTA = 1,4,7,10-Tetraazacyclododecane-N,N',N'',N'''-tetraacetic Acid), *Inorg. Chem*. 1994, **33**, 4048.

74 J. C. P. Grancho, M. M. Pereira, M. da G. Miguel, A. M. Rocha Gonsalves, H. D. Burrows, Synthesis, spectra and photophysics of some free base tetrafluoroalkyl and tetrafluoroaryl porphyrins with potential applications in imaging, Photochem. Photobiol., 2002, **75**, 249.

75 P.A. Tanner, Some misconceptions concerning the electronic spectra of tri-positive europium and cerium, *Chem. Soc. Rev.*, 2013, **42**, 5090.

76 K. Binnemans, Interpretation of europium (III) spectra, *Coord. Chem. Rev.*, 2015, **295**, 1.

77 S. Aime, M. Botta, M. Fasano, M.P.M. Marques, C.F.G.C. Geraldes, D. Pubanz, A.E. Merbach, Conformational and coordination equilibria on DOTA complexes of lanthanide metal ions in aqueous solution studied by (1)H-NMR Spectroscopy, *Inorg. Chem.* 1997, **36**, 2059.

78 J.A. Peters, K. Djanashvili, C.F.G.C. Geraldes, C. Platas-Iglesias, in *The Chemistry of Contrast Agents in Medical Magnetic Resonance Imaging*, Ed. A. Merbach, L. Helm and É. Tóth, Wiley, 2nd Edition, 2013, p. 209.

79 M. Latva, H. Takalo, V.-M. Mukkala, C. Matachescu, J. C. Rodriguez-Ubis, J. Kankare, Correlation between the lowest triplet state energy level of the ligand and lanthanide(III) luminescence quantum yield, *J. Lumin.* 1997, **75**, 149.

80 M. Momtaldi, A. Credi, L. Prodi, M. T. Gandolfini, *Handbook of Photochemistry*, Taylor & Francis, N. Y., 2006.

81 O.L. Malta, Mechanisms of non-radiative energy transfer involving lanthanide ions revisited, *J. Non-Cryst. Solids* 2008, **354**, 4770.

82 G.F. de Sá, O.L. Malta, C. de Mello Donegá, A.M. Simas, R.L. Longo, P.A. Santa-Cruz, E.F. da Silva Jr., Spectroscopic properties and design of highly luminescent lanthanide coordination complexes, *Coord. Chem. Rev*. 2000, **196**, 165.

83 A.N.C. Neto, E.E.S. Teotónio, G.F. de Sá, H.F. Brito, J. Legendziewicz, L.D. Carlos, M.C.F.C. Felinto, P. Gawryszewska, R.T. Moura Jr, R.L. Longo, W.M. Faustino, O.L. Malta, in *Handbook on the Physics and Chemistry of Rare Earths*, eds. J.-C. G. Bünzli and V. K. Pecharsky, Elsevier B.V., Amsterdam, The Netherlands, 2019, **56**, p. 55.

84 S. Hassoon, H. Lustig, M. B. Rubin, S. Speiser, The mechanism of short-range intramolecular electronic energy transfer in bichromophoric molecules, *J. Phys. Chem.*, 1984, **88**, 6367.

85 S. V. Eliseeva, J.-C. G. Bünzli, Lanthanide luminescence for functional materials and bio-sciences, *Chem. Soc. Rev.* 2010, **39**, 189.

86 J.-C. G. Bünzli, Lanthanide light for biology and medical diagnosis, *J. Lumin.* 2016, **170**, 866.

87 M. H. V. Werts, R. T. F. Jukes, J. W. Verhoeven, The emission spectrum and the radiative lifetime of Eu3+ in luminescent lanthanide complexes, *Phys. Chem. Chem. Phys.* 2002, **4**, 1542.

88 A. Beeby, L. M. Bushby, D. Maffeo, G. J. A. Williams, Intramolecular sensitisation of lanthanide(III) luminescence by acetophenone-containing ligands: the critical effect of para-substituents and solvent, *J. Chem. Soc., Dalt. Trans.*, 2002, 48.

89 S. Quici, M. Cavazzini, G. Marzanni, G. Accorsi, N. Armaroli, B. Ventura, F. Barigelletti, Visible and Near-Infrared Intense Luminescence from Water-Soluble Lanthanide [Tb(III), Eu(III), Sm(III), Dy(III), Pr(III), Ho(III), Yb(III), Nd(III), Er(III)] Complexes, *Inorg. Chem.*, 2005, **44**, 529.

90 W. D. Horrocks, D. R. Sudnick, Lanthanide ion luminescence probes of the structure of biological macromolecules, *Acc. Chem. Res.*, 1981, **14**, 384.

91 A. Beeby, I. M. Clarkson, R. S. Dickins, S. Faulkner, D. Parker, L. Royle, A. S. de Sousa, J. A. G. Williams, M. Woods, Non-radiative deactivation of the excited states of europium, terbium and ytterbium complexes by proximate energy-matched OH, NH and CH oscillators: an improved luminescence method for establishing solution hydration states, *J. Chem. Soc., Perkin Trans. 2*, 1999, 493.